Macromolecules
ARTICLE

*Macromolecules* **2010**, *43*, 2535–2543 **2535**
DOI: 10.1021/ma901369a

# Analysis of the Migration of Rigid Polymers and Nanorods in a Rotating Viscometric Flow

**Joontaek Park and Jason E. Butler***

*Department of Chemical Engineering, University of Florida, Gainesville, Florida 32611*

*Received June 25, 2009; Revised Manuscript Received January 4, 2010*

ABSTRACT: The dynamics and rheology of a rigid polymer or nanorod suspended in a Newtonian, viscous fluid under torsional flow have been studied. Our theoretical analysis predicts that rigid rods migrate in the radial direction according to their orientational configuration which is controlled by the competition between the shear flow, which tends to align the rods in the direction of flow, and Brownian motion, which tends to randomize the orientation. Steady and transient distributions of the center-of-mass in a dilute solution are derived from a kinetic theory and are confirmed by performing a Brownian dynamics simulation. The migration shifts the distribution toward the axis of rotation and enhances the shear-thinning behavior of the suspension.

## Introduction

Processing of suspensions of rigid polymers and Brownian rods, in the form of short lengths of biopolymers and nanotubes, occurs in many applications. Likewise, rheological testing is being applied more widely to characterize suspensions of nanotubes, including materials such as carbon nanotubes.[1−4] Yet, the dynamics of rigid rods remains largely unexplored even in the simplest of systems. Consequently, the prediction of behaviors and interpretation of measurements are significantly hindered.

For example, observations[5−8] of the rheology of semidilute suspensions of rigid rods indicate the existence of measurable shear thinning even for experimental systems where the Peclet number is very large. Such reductions are not predicted by theoretical and numerical evaluations of the stress at infinite Peclet number,[9−13] indicating that the finite, though relatively small, Brownian fluctuations may be playing a significant role in causing the shear thinning. The shear rate dependence observed in some specific experiments may be accounted for by deviations of the experimental systems from model systems, such as flexibility[14] and adhesion between the rods.[6] However, a clear explanation of the shear thinning phenomenon is lacking.

Kinetic theory calculations presented here predict that rigid rods suspended in rotational viscometric flows can experience a net migration when sheared at large, but finite, values of the Peclet number. The specific case of torsional flow, or the flow generated between two parallel plates where one plate is rotated relative to the other, is studied. A net migration of rods in the radial direction arises from a coupling of the curvature of the flow field and the mean orientation of the polymers, which is set by a balance between the local value of the shear rate and the Brownian rotation. The distribution of polymers gradually shifts toward the central axis of the spinning disks and eventually results in a distribution that is strongly concentrated near the axis of rotation of the parallel plates. The migration reduces the particle contribution to the measured viscosity as compared to an assumption that the distribution is uniform and may in part explain the large and unexpected shear thinning in at least one set of experiments.[8]

*Corresponding author. E-mail: butler@che.ufl.edu.

The mechanism of migration of the rigid rod is analogous to that of the migration of a flexible polymer in a similar, inhomogeneous velocity field. For a flexible polymer suspended in rotating flows in the Stokes regime, studies[15−18] have shown that flexible polymers in rotating flows migrate toward the axis of rotation, resulting in inhomogeneous distributions. For rigid polymers, Aubert and Tirrell (1980) and Aubert et al. (1980) speculated that a similar migration would happen for ellipsoids in inhomogeneous velocity fields, citing a formula predicting motions of rigid ellipsoids.[19,20] However, quantitative and qualitative analyses of the dynamics of migration, center-of-mass distribution, and particle stress contribution of rigid polymers in inhomogeneous velocity fields, such as rotating flows, have not been made.

Note that the mechanism reported here appears distinct from other investigations of the migration of rigid spheres[21−25] and rods[25] in torsional flows. These have shown that inertia and viscoelasticity can cause radial migration. However, these effects are beyond the limits of investigation of this work since the Brownian rods are assumed to be suspended in a Newtonian fluid and sheared in the limit of zero Reynolds number. The equation of motion which considers these limits and the inhomogeneous flow field is derived. Prediction of the steady and unsteady center-of-mass distributions in the radial direction are made using the equation of motion, and the particle stress contribution is evaluated from the resulting distributions.

## Center-of-Mass Distribution

We model a rigid polymer or nanorod in a torsional flow, as illustrated in Figure 1. The suspending fluid is Newtonian, and the Reynolds number is assumed to be sufficiently small to neglect any inertial effects. The neutrally buoyant rod is acted upon by hydrodynamic and Brownian forces only. Similar to approximations made in theories for the migration of a flexible polymer[26,27] and a rigid polymer[28] in rectilinear flow, steric and hydrodynamic interactions of the rod with the boundaries are assumed to not influence the rotation of the rod. We also ignore the effect of hydrodynamic interactions with the boundaries for the center-of-mass motion. The concentration of the rod in this system is assumed to be dilute; therefore, only the motion of a


Published on Web 02/04/2010

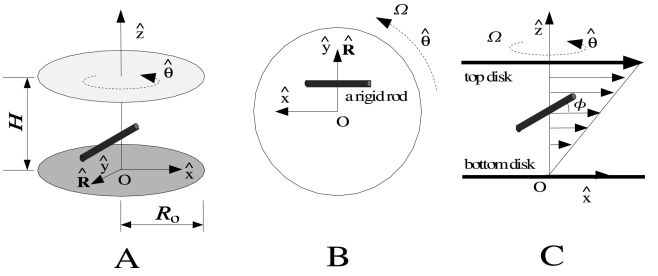


**Figure 1.** Schematic diagrams of torsional flow in (A) Cartesian coordinates and cylindrical coordinates and in views from (B) the *xy*-plane and (C) the *xz*-plane. Unit vectors in each direction are indicated as $\hat{\mathbf{x}}$, $\hat{\mathbf{y}}$, $\hat{\mathbf{z}}$, $\hat{\boldsymbol{\theta}}$, and $\hat{\mathbf{R}}$. The Cartesian coordinates are set so that the center-of-mass of the rigid rod is located at $\mathbf{r} = (0,R,r_z)$.

single rod in a torsional flow is considered. Furthermore, the center-of-mass distribution in the angular and *z*-directions are assumed to be uniform and the center-of-mass distribution in the radial direction will be derived.

The mean evolution of a rigid rod in torsional flow, as illustrated in Figure 1, is governed by a continuity equation for the distribution function, $\Psi(\mathbf{r},\mathbf{p},t)$

$$\frac{\partial \Psi}{\partial t} = -\nabla\cdot(\dot{\mathbf{r}}\Psi) - \nabla_{\mathbf{p}}\cdot(\dot{\mathbf{p}}\Psi) \tag{1}$$

where $t$ is time, $\mathbf{r}$ is the center-of-mass position of a rod, and $\mathbf{p}$ is the orientation or unit vector that parallels the rod's major axis. The center-of-mass velocity is $\dot{\mathbf{r}}$, and $\dot{\mathbf{p}}$ is the rotational velocity or time evolution of $\mathbf{p}$. The gradient with respect to orientation can be written as[29,30]

$$\nabla_{\mathbf{p}} = (\mathbf{I}-\mathbf{pp})\cdot\frac{\partial}{\partial \mathbf{p}} \tag{2}$$

where $\mathbf{I}$ is the identity matrix. The distribution $\Psi$ is written as a product of a center-of-mass, $n$, and orientation, $\psi$, distribution

$$\Psi(\mathbf{r},\mathbf{p},t) = n(\mathbf{r},t)\psi(\mathbf{r},\mathbf{p},t) \tag{3}$$

where $n = \int \psi \, d\mathbf{p}$. The steady-state center-of-mass distribution $n$ is obtained by integrating eq 1 over the orientation distribution

$$0 = \nabla\cdot(n\langle\dot{\mathbf{r}}\rangle) \tag{4}$$

where the angle bracket $\langle ...\rangle$ indicates an ensemble average over orientation, $\int ...\psi \, d\mathbf{p}$.

At steady state, the orientation distribution satisfies

$$0 = -\nabla\cdot(n\dot{\mathbf{r}}\psi) - n\nabla_{\mathbf{p}}\cdot(\dot{\mathbf{p}}\psi) \tag{5}$$

Approximating $n\dot{\mathbf{r}}\psi$ by $n\langle\dot{\mathbf{r}}\rangle$ within eq 5 and using eq 4 gives

$$0 = \nabla_{\mathbf{p}}\cdot(\dot{\mathbf{p}}\psi) \tag{6}$$

This approximation relies on the fact that the orientation distribution of the rods equilibrates much faster than their center-of-mass migrates and diffuses across streamlines. Though possible to calculate $\psi$ more accurately by a process of successive substitution,[27] the approximation has been used with success to model similar systems of elastic dumbbells[26,27] and rigid rods[28,31] where the rate of transfer is much slower than the relaxation rate of the end-to-end vector or orientation, respectively. The approximation has been validated in these previous works by comparing with simulations; similarly, the results of the Brownian dynamics simulation described in the Appendix are used to validate the use of the approximation for this specific case as well.

Equation 6 will be solved to give $\psi$ for use in the evaluation of $\langle\dot{\mathbf{r}}\rangle$. However, determining $n$ from eq 4 first necessitates an explicit expression for $\dot{\mathbf{r}}$. Such an expression is developed in the next section.

**Drift in the Radial Direction.** Figure 1 illustrates a torsional flow, where a Newtonian fluid between two parallel disks of equal radii $R_0$ and separated by a gap $H$ is sheared by rotating the top disk with angular velocity $\Omega$. In cylindrical coordinates, the $z$-direction defines the axis of rotation and the unit vectors $\hat{\mathbf{R}}$ and $\hat{\boldsymbol{\theta}}$ indicate the radial and angular directions, respectively. The origin $O$ is located at the center of the bottom, stationary disk.

We use the slender-body approximation[32−34] to model the motion of a rigid Brown rod of high aspect ratio $A \geq 10$ in this flow field. Here, the aspect ratio $A$ is defined as the ratio of the length of the major axis, $L$, to the minor axis, $d$. The center-of-mass velocity, $\dot{\mathbf{r}}$, is given by

$$\dot{\mathbf{r}} = \frac{1}{L}\int_{-L/2}^{L/2} \mathbf{u}(\mathbf{r}+s\mathbf{p})\, ds + \xi^{-1}(\mathbf{I}+\mathbf{pp})\cdot\mathscr{F} \tag{7}$$

where $\mathbf{u}$ is the flow field, the coordinate $s$ describes positions along the axis such that $-0.5L \leq s \leq 0.5L$, and $s = 0$ is the center-of-mass. The Brownian force, $\mathscr{F}$, acting on the rod is balanced by the hydrodynamic forces to give eq 7. The leading order term in the resistance coefficient of a rigid rod as approximated by slender-body theory is

$$\xi = \frac{4\pi\mu L}{\ln(2A)} \tag{8}$$

where $\mu$ is the viscosity of the Newtonian suspending fluid.

The flow field of the torsional flow between the two parallel plates as expressed in Cartesian coordinates and shown in Figure 1 is

$$\mathbf{u}(\mathbf{x}) = -\frac{\dot{\gamma}_0}{R_0} z[-y\hat{\mathbf{x}} + x\hat{\mathbf{y}}] \tag{9}$$

where $\mathbf{x} = (x,y,z)$ is a point in the flow field and the shear rate at the edge of the disk is defined as

$$\dot{\gamma}_0 = \dot{\gamma}(R_0) = \frac{\Omega}{H}R_0 \tag{10}$$

For convenience, the coordinate system is defined to rotate with the center-of-mass of the rod, with the $y$-direction corresponding to the radial direction. As a result, the $y$-coordinate of the center-of-mass is specified by the radial distance $R$ of the rod's center from the axis of rotation of the torsional flow and the $x$-position of the center-of-mass equals zero. The center-of-mass is specified by $\mathbf{r} = (0,R,r_z)$, where $r_z$ is the center of mass coordinate in the $z$-direction as measured from the bottom plate.

Using these definitions, the velocity of the torsional flow evaluated at any point $s$ along the centerline of the rod can be written as

$$\mathbf{u}(\mathbf{r}+s\mathbf{p}) = -\frac{\dot{\gamma}_0}{R_0}(r_z+sp_z)[-(R+sp_y)\hat{\mathbf{x}} + sp_x\hat{\mathbf{y}}] \tag{11}$$

where $\mathbf{p} = (p_x,p_y,p_z)$. Hence, integrating $u_y$, the $y$-component of eq 11, along the centerline of the rod as indicated in the first term of eq 7 gives the radial velocity of the rod

$$U_D = \frac{1}{L}\int_{-L/2}^{L/2} u_y(\mathbf{r}+s\mathbf{p})\, ds$$

$$= -\frac{\Omega}{LH}\int_{-L/2}^{L/2}(r_z+sp_z)sp_x\, ds = -\frac{\dot{\gamma}_0 L^2}{12R_0}p_x p_z \tag{12}$$

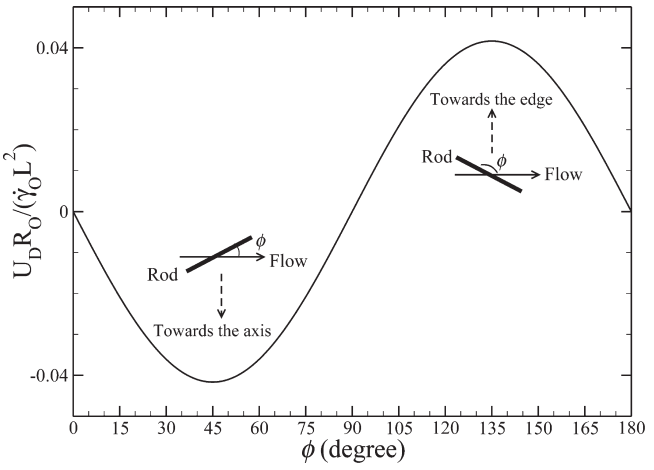


**Figure 2.** Drift $U_D$ of a rigid rod with $p_y = 0$ in a torsional flow as a function of $\phi$ is proportional to $\dot{\gamma}_0 L^2/R_0$. Negative velocities indicate a drift toward the rotational axis ($R = 0$). Insets illustrate the relation between the direction of the drift $U_D$ and $\phi$.

This is the drift velocity of the rigid rod, $U_D$, due to the inhomogeneous velocity field.

Equation 12 predicts the dependence of the drift on rod orientation as shown in Figure 2. A rigid rod moves either toward the rotational axis ($R = 0$) or the edge ($R = R_0$) depending upon the instantaneous orientation. Since the orientation distribution of a non-Brownian, slender-body that is tumbling in the torsional flow is symmetric about the flow direction in the absence of interactions with the bounding walls, such a rod does not experience a net migration. Indeed, experimenters[25] did not observe migration of non-Brownian rods suspended in a Newtonian fluid undergoing torsional flow. However, a Brownian rod has an asymmetric orientation distribution due to the competition between the shear flow, which tends to align the rod with the flow direction, and Brownian motion, which tends to randomize the orientation.[35] It will be shown that the broken symmetry of the orientation distribution produces an average angle of small positive value, which drives a migration toward the rotational axis as seen in Figure 2.

As long as the assumption that orientation is not affected by the boundaries holds, the drift velocity $U_D$ depends on the instantaneous orientation only, but not the center-of-mass position, according to eq 12. The lack of dependence on $R$ arises from a cancellation of two radial effects. For rods closer to the rotational axis ($R = 0$), the influence of the rotational, or deviation from a strictly rectilinear, flow becomes stronger. Analysis shows that if the local shear rate is held constant regardless of position $R$, the drift velocity should scale as $1/R$. However, the local value of shear rate does vary in the parallel-plate geometry as $R$, and since the drift velocity is proportional to the local shear rate, the two dependencies cancel. Combination of the drift (eq 12) with Brownian displacements of the center-of-mass in the $y$-direction gives the expression for the motion that will be used in solving eq 4

$$\dot{R} = -\frac{L^2\dot{\gamma}_0}{12R_0}p_x p_z + \xi^{-1}(\hat{\mathbf{y}} + p_y\mathbf{p})\cdot\mathscr{F} \tag{13}$$

where $\dot{R}$ is the $y$-component of $\dot{\mathbf{r}}$.

**Distribution at Steady State.** The radial distribution at steady state is governed by a simplified version of eq 4

$$0 = -\frac{1}{R}\frac{\partial}{\partial R}(nR\langle\dot{R}\rangle) \tag{14}$$

where the flux is calculated using eq 13

$$n\langle\dot{R}\rangle = -n\frac{L^2\dot{\gamma}_0}{12R_0}\langle p_x p_z\rangle + \frac{n}{\xi}\langle(\hat{\mathbf{y}} + p_y\mathbf{p})\cdot[-k_B T\nabla \ln \Psi]\rangle \tag{15}$$

The Brownian force has been written as the gradient of the potential of mean force,[30] $\mathscr{F} = -k_B T\Delta \ln \Psi$. Further simplification of the second term, making use of the property $\Psi = n\psi$ (eq 3), gives

$$n\langle\dot{R}\rangle = -n\frac{L^2\dot{\gamma}_0}{12R_0}\langle p_x p_z\rangle - \frac{k_B T}{\xi}\left[(1 + \langle p_y{}^2\rangle)\frac{\partial n}{\partial R} + n\frac{\partial\langle p_y{}^2\rangle}{\partial R}\right] \tag{16}$$

The net radial flux at every position $R$ must be zero at steady state. Consequently, setting eq 16 to zero and rearranging gives the differential equation

$$\frac{\partial \ln n}{\partial R} = \frac{\langle K\rangle + \langle\Gamma\rangle}{1 + \langle p_y{}^2\rangle} \tag{17}$$

where

$$\langle K\rangle = -\frac{Pe_0}{R_0}\langle p_x p_z\rangle, \quad \langle\Gamma\rangle = -\frac{\partial\langle p_y{}^2\rangle}{\partial R} \tag{18}$$

and $Pe_0$ is the value of the rotary Péclet number evaluated at the edge of the plates

$$Pe_0 = \frac{\dot{\gamma}_0\xi L^2}{12k_B T} \tag{19}$$

Comparing the migration mechanism identified in this theory to that of flexible polymers,[17] the term $\langle K\rangle$ is analogous to the migration term for flexible polymers which relates the migration to the inhomogeneous velocity field of the torsional flow. The average drift term of a flexible polymer also contains the average moments of its end-to-end vector in the plane of shear, which represents the balance between the spring force and the shear flow. For a rigid rod, the average moment $\langle p_x p_z\rangle$ is determined by the balance between the Brownian rotation and the shear flow.

The term $\langle\Gamma\rangle$ is related to the gradient of the anisotropic mobility of a rigid rod. Hence, it is similar to the so-called anisotropic diffusivity term which causes a migration of rigid rods in pressure-driven flow.[36,37] The term $\langle\Gamma\rangle$ arises from consideration of hydrodynamic interactions between portions of a rod as implicitly included within the slender-body approximation. In the analysis of flexible polymers using the bead−spring model,[17] hydrodynamic interactions between the beads were neglected, and no term corresponding to $\langle\Gamma\rangle$ was produced for migration of flexible polymers as a result.

Integration of eq 17 over $R$ gives the center-of-mass distribution in the radial direction, but the position-dependent values of the orientation moments must be obtained by integrating over the orientation distribution function, $\psi$, from eq 6. Solving eq 6 requires the equation of motion for the rotation of a rigid slender-body[38,39]

$$\dot{\mathbf{p}} = \frac{12}{L^3}(\mathbf{I} - \mathbf{pp})\cdot\int_{-L/2}^{L/2} s\mathbf{u}(\mathbf{r} + s\mathbf{p})\,\mathrm{d}s + \frac{12}{\xi L^2}\mathscr{T}\times\mathbf{p} \tag{20}$$

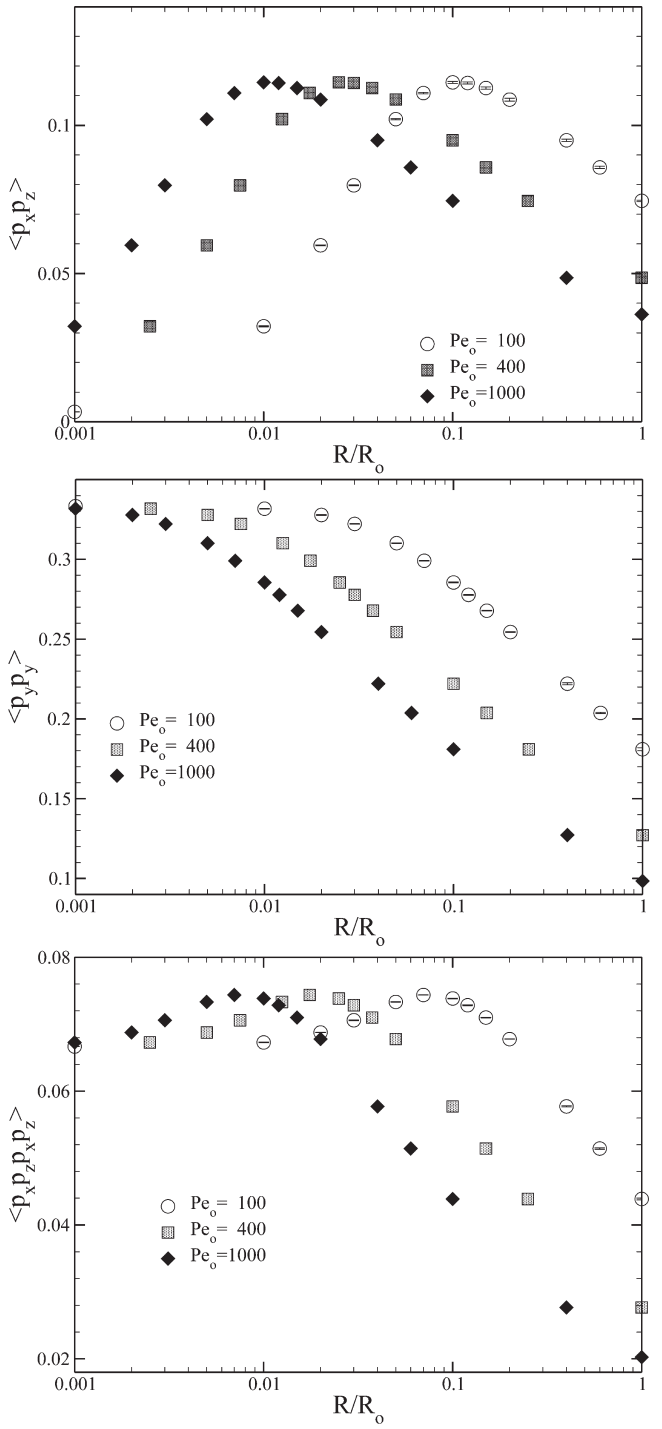


**Figure 3.** Average orientation moments of a rigid rod in torsional flows at three $Pe_0$ as a function of $R/R_0$.

where $\mathscr{T}$ is the Brownian torque acting on the rod. Substitution of **u** as defined in eq 11 gives

$$\dot{\mathbf{p}} = \frac{\dot{\gamma}_0}{R_0} R p_z (\hat{\mathbf{x}} - p_x \mathbf{p}) + \frac{12}{\xi L^2} \mathscr{T} \times \mathbf{p} \qquad (21)$$

The first term on the right-hand side corresponds to the change of the orientation due to shear flows of rate $\dot{\gamma}(R) = \dot{\gamma}_0 R/R_0$ in the $x$-direction with the gradient in the $z$-direction. This term indicates that the orientation distribution depends on the local shear rate which varies linearly with $R$. Note that the rotational dynamics of a slender body in a torsional flow

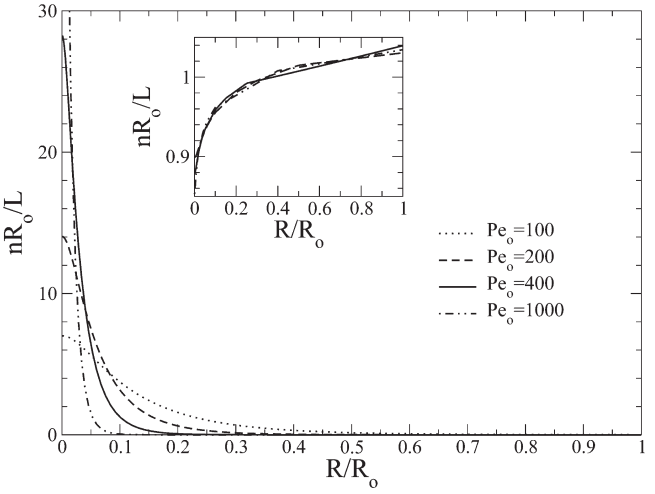


**Figure 4.** Steady-state center-of-mass distributions of a rigid rod in torsional flow as a function of $R/R_0$ and $Pe_0$. Inset shows the distributions when considering only the migration arising from the anisotropic diffusivity. The distribution function $n$ is normalized such that $\int n \, dR = 1$ and is scaled by $L/R_0$.

with a center-of-mass held at a position $R$ is identical to that in a simple shear flow of rate $\dot{\gamma}(R)$.

The average orientation moments of a rigid rod at $\mathbf{r} = (0,R,r_z)$ in torsional flows of various $Pe_0$ are obtained by performing Brownian dynamics simulations[40] rather than integrating eq 6 directly. The averaging of sampled orientation moments is performed over 1000 simulation time increments of $5\dot{\gamma}_0^{-1}$. The number of samples taken within each increment of time was $10^4$. This level of averaging was repeated five times using different initial conditions to arrive at the final averaged value of the moments; the standard deviations of the results shown in Figure 3 are smaller than the size of the symbols. Three orientation moments are displayed: $\langle p_y^2 \rangle$ and $\langle p_x p_z \rangle$ are used for integration of eq 17 and $\langle p_x^2 p_z^2 \rangle$ will be used in the calculation of stresses. As $Pe_0$ changes, the average orientation moments shift according to the local value of the Péclet number, $Pe(R) = RPe_0/R_0$.

Figure 4 shows the center-of-mass distributions determined by numerically integrating eq 17 using Gauss–Legendre quadrature. The average orientation moments at each integration point are obtained by interpolating the numerical results shown in Figure 3. The steady distributions, when scaled by $L/R_0$ and plotted versus $R/R_0$, are a function only of $Pe_0$ as shown. The center-of-mass distribution concentrates more strongly toward the axis as $Pe_0$ increases. As in simple shear flow, Brownian rotation breaks the symmetry of orientation distribution to give positive values of $\langle p_x p_z \rangle$, which induces migration toward the axis within the torsional flow as predicted by eq 13.

A migration toward the axis is found from similar theories for a flexible polymer,[17] though comparisons indicate that the extent of migration for the rigid rod is less than that of the flexible polymer at similar values of the shear rate. The reduced migration of the rigid rod is not attributable to the contributions from $\langle \Gamma \rangle$ in eq 17. Though this term generates migration away from the axis since the gradient of $\langle p_y^2 \rangle$ is negative, the effect of $\langle \Gamma \rangle$ is too weak to visibly influence the observed distribution when including $\langle K \rangle$. The inset of Figure 4 shows the distribution obtained by integrating eq 17 with $\langle \Gamma \rangle$, but without the inhomogeneous velocity field term $\langle K \rangle$. The result shows that the distribution is a nearly uniform one as compared to the solution which includes both $\langle \Gamma \rangle$ and $\langle K \rangle$.

**Time Evolution of Distributions.** The evolution of the center-of-mass distribution is obtained from the time-dependent version of eq 4

$$\frac{\partial n}{\partial t} = -\frac{1}{R}\frac{\partial}{\partial R}(nR\langle \dot{R}\rangle) \tag{22}$$

where $\langle \dot{R}\rangle$ can be evaluated from eq 16 by assuming that the orientation distribution equilibrates rapidly compared to the radial migration of the center-of-mass. Consequently, the average orientation moments required for $\langle \dot{R}\rangle$ at each position and moment in time can be obtained by interpolating the data shown in Figure 3. Solving eq 22 numerically using the Crank−Nicolson scheme with the boundary condition of no net flux at $R = R_0$ gives the transient distribution of the center-of-mass. Starting from an initially uniform distribution, the distribution in torsional flows with $R_0 = 100L$ develops as shown in Figure 5. A time step of $\dot{\gamma}_0^{-1}$ and spatial resolution of $0.1L$ are sufficiently small to give convergent numerical results.

As time proceeds, the distribution near the axis rapidly increases while that far from the axis declines as compared to the initial value. After a time comparable to $10^6\dot{\gamma}_0^{-1}$, the distribution becomes nearly identical to the steady-state distribution. The time to achieve steady state, $t_s$, can be approximated as the time for a rod to travel a distance $R_0$ at a velocity equivalent to the mean value of the drift velocity, $\langle U_D\rangle$. Using the rough estimate of $\langle p_x p_z\rangle \approx 0.06$, as determined from data in Figure 3, gives a time to steady state of approximately

$$t_s \sim 2\left(\frac{10R_0}{L}\right)^2 \dot{\gamma}_0^{-1} \tag{23}$$

This scaling agrees with the results of simulations for $R_0 = 100L$, which gives $t_s \sim O(10^6)\dot{\gamma}_0^{-1}$, and the effect of changing $Pe_0$ from $10^2$ to $10^3$ results in a small difference in $t_s$.

Brownian dynamics simulations, performed at $Pe_0 = 100$ as described in the Appendix, are also shown in Figure 5. Small discrepancies between the simulation and theoretical results exist near the rotational axis ($R_0 = 0$) at short times, but the simulation results are in agreement within the error bars over the vast majority of the radius of the plates and at long times. This good agreement confirms that the approximation made in obtaining eq 6 and eq 22, as discussed following eq 6, does not adversely affect the prediction of the radial distribution of the rods.

**Discussion of Boundary Effects.** In this study, hydrodynamic and steric interactions between rigid rods and the boundaries are not considered. We discuss the possible effects of the boundaries and the concentration, which were also ignored in previous studies for a flexible polymer,[15−18] on the results.

Derivation of eq 17 utilizes approximations that the orientation distribution is not influenced by the boundaries and is separable from the center-of-mass distribution. Though the latter approximation was validated using Brownian dynamics simulations as shown in Figure 5, the Brownian dynamics simulations did not consider the steric effects of the boundaries. Integration of eq 17 to produce Figure 4 excludes regions very near the boundaries. However, near the edge ($R_0 - R < 0.5L$), $n$ approaches 0 at high $Pe_0$ so ignoring the boundary at $R_0$ negligibly impacts the predicted distributions.

The interaction of the rods with the disks at $z = 0$ and $H$ can induce depletion layers that extend a distance of $L/2$ and higher into the fluid, depending upon the Peclet number. Excluded volume interactions of the rod with the disks create depletion layers of approximately one-half of a rod length[37,41] at low to moderate values of $Pe \sim O(10^2)$. Hydrodynamic coupling of the rods with the disks at high $Pe$ also drives a net migration across the gap and results in a larger depletion layer.[28,31] This nonuniform distribution across the gap should have no effect on the extent of the radial migration. However, changes to the orientation distribution resulting from the interactions with the walls of the disks could alter the radial migration according to eq 13. The hydrodynamic interactions do not change the orientation significantly, but excluded volume alters the orientation for those rods located within a distance of $L/2$ of the disk walls. Relatively few rods would be in this range for $H \gg L$, so the effect upon the radial distribution is presumably minor.

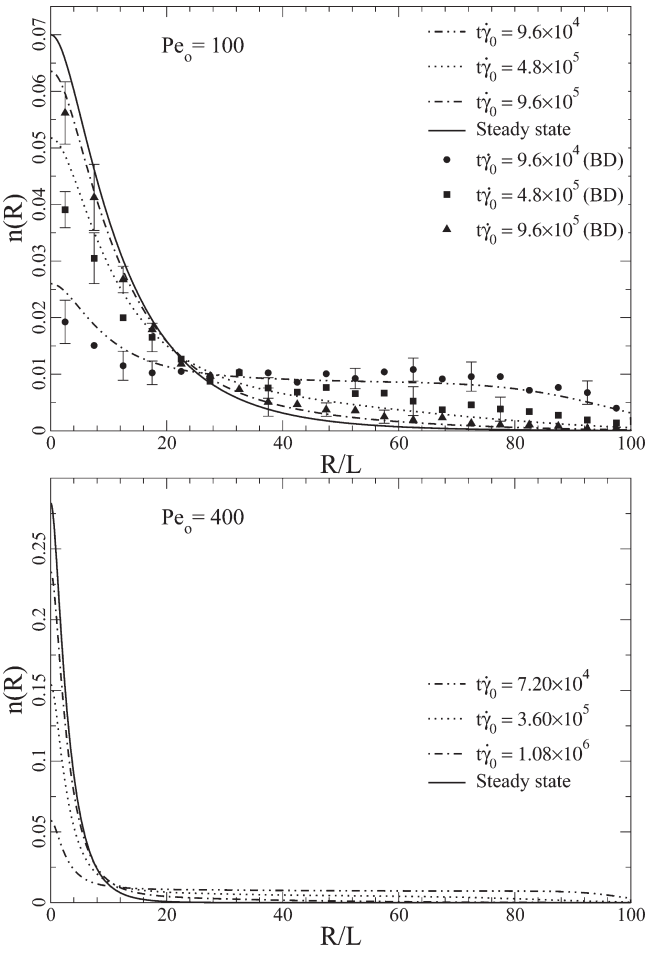


**Figure 5.** Time-dependent center-of-mass distributions of a rigid rod in torsional flows of $Pe_0 = 100$ and $Pe_0 = 400$ with $R_0 = 100L$. Theoretical predictions are indicated by lines and Brownian dynamics (BD) simulation results are plotted as symbols.

The dilute approximation could likely be inappropriate near the rotational axis ($0 < R < 0.5L$) where the center-of-mass distribution is maximum, even for an initially dilute concentration. The steric interactions between the rods would generally lower the extent of migration through a direct exclusion mechanism. The steric and hydrodynamic interaction would also indirectly alter the orientation distribution and, hence, the average drift velocity; the effect of this indirect mechanism is harder to anticipate. Hence, studies comparing the experimental results and simulations that include interactions between rods would improve the prediction of the distribution.

### Stress Calculation

The migration of rods within the torsional flow will influence measurements of stress when performing rheological characterization of these systems within parallel-plate geometries. In this section, we calculate the steady and time-dependent stress due to the migration of the rods and compare with the stress measured when assuming a uniform distribution of the center-of-mass. The calculation of the particle stress given here utilizes a dilute approximation; no rod influences the flow or interacts directly with any other rod. However, the migration strongly concentrates particles near the axis, so even an initially dilute suspension may violate the dilute approximation as time progresses. Still, the calculation given here serves to demonstrate the large effect that the migration can potentially have on the measurement of particle stress.

Stresses and viscosities in a parallel plate device are typically reported in terms of the value of the shear rate at the edge of the plates, $\dot{\gamma}_0$. The stress at rate $\dot{\gamma}_0$ is[42]

$$\sigma(\dot{\gamma}_0) = 2\overline{\sigma} + \dot{\gamma}_0 \frac{\partial \overline{\sigma}}{\partial \dot{\gamma}_0} \tag{24}$$

where $\bar{\sigma}$ is the average of the position dependent stress, $\sigma(\mathbf{x})$, over the volume $V$ of fluid between the plates

$$\overline{\sigma} = \frac{1}{V}\int \sigma \, \mathrm{d}V \tag{25}$$

The stress $\sigma$ depends on the local value of the shear rate and contains contributions from the Newtonian suspending fluid of viscosity $\mu$ and the particles. Averaging as designated in eq 25 and substituting the result into eq 24 gives the stress as evaluated at the edge of the plates

$$\sigma(\dot{\gamma}_0) = -P\mathbf{I} + 2\mu\mathbf{E} + \sigma^P(\dot{\gamma}_0) \tag{26}$$

where $P$ is the pressure and $\mathbf{E}$ is the rate of strain tensor. Here, the first two contributions in eq 26 are those expected for a Newtonian fluid. The last term is the contribution of the dilute suspension of rods to the stress as given by $\sigma^P(\dot{\gamma}_0) = 2\bar{\sigma}^P + \dot{\gamma}_0(\partial\bar{\sigma}^P/\partial\dot{\gamma}_0)$.

The mean particle contribution, $\bar{\sigma}^P$, requires evaluation of the stresslet, $\mathbf{S}$, of each particle. Since the stresslet depends on the configuration of the rods, averaging $\mathbf{S}$ over the expected configuration in the system of volume $V$ gives the mean particle stress contribution

$$\overline{\sigma}^P = n_\mathrm{d}\iint \Psi \mathbf{S} \, \mathrm{d}\mathbf{p} \, \mathrm{d}V \tag{27}$$

where $n_\mathrm{d}$ is the bulk number density of particles in the volume $V$. Note that this procedure for calculating the particle contribution to the stress assumes that each particle contributes to the stress at the position of its center-of-mass. This assumption of a local rheology is not strictly accurate; calculating the stress from a nonlocal theory[43,44] would be preferable. However, the approximation is not severe so long as the flow field varies little over the length of the rod as is the case for $L \ll R_0$. The stresslet for a rigid slender body suspended in a Newtonian fluid is given by[9]

$$\mathbf{S} = -\int_{-L/2}^{L/2}\left[\mathbf{f}(s)\mathbf{p} - \frac{1}{3}\mathbf{I}\{\mathbf{f}(s)\cdot\mathbf{p}\}\right] s \, \mathrm{d}s \tag{28}$$

Here, $\mathbf{f}(s)$ is the line force distribution on a rod and is derived for torsional flow from eq 2.11 of ref 39 using the flow field given in eq 9

$$\mathbf{f}(s) = \frac{1}{L}\mathscr{T} + \frac{12s}{L^3}[\mathscr{T}\times\mathbf{p} + S\mathbf{p}] + \frac{\Omega\xi}{HL}p_z\left(s^2 - \frac{L^2}{12}\right)(p_y\hat{\mathbf{x}} - p_x\hat{\mathbf{y}}) \tag{29}$$

where $\mathscr{T}$ is the torque on the rod and the stresslet coefficient is given by

$$S = -\frac{\xi}{2L}\int_{-L/2}^{L/2} s\mathbf{p}\cdot\mathbf{u}(s) \, \mathrm{d}s \tag{30}$$

Performing the integration indicated in eq 28 using eq 29 gives

$$\mathbf{S} = -(\mathscr{T}\times\mathbf{p})\mathbf{p} - S\left(\mathbf{pp} - \frac{1}{3}\mathbf{I}\right) \tag{31}$$

Note that the same approximations used in solving eq 1 are also applied in this evaluation of the stress. Hence, orientations in eq 31 are affected only by the flow and the Brownian torque. Consequently, the torque $\mathscr{T}$ in eq 31 contains contributions only from Brownian motion.

The Brownian torque in eq 31 is replaced with the gradient of the potential of mean torque in terms of the thermal energy and distribution function[30]

$$\mathscr{T}\times\mathbf{p} = -k_\mathrm{B}T(\mathbf{I} - \mathbf{pp})\cdot\frac{\partial \ln \Psi}{\partial \mathbf{p}} \tag{32}$$

The stresslet coefficient for a rigid rod in a torsional flow as in Figure 1 is obtained from eq 9 and eq 30

$$S = \frac{\pi L^3 \mu\dot{\gamma}(R)}{6\ln(2A)}p_x p_z \tag{33}$$

which is identical to the stresslet coefficient in a simple shear flow of rate $\dot{\gamma}$, except the shear rate is position dependent in this case.

Substitution of eq 32 and eq 33 into eq 31 gives the stresslet of a Brownian rod in a torsional flow. For integrating the stresslet using eq 27, the distribution function is factorized ($\Psi = n\psi$) and an average over the orientation distribution is made

$$\overline{\sigma}^P = n_\mathrm{d}\int\langle\mathbf{S}\rangle n \, \mathrm{d}V = 2\pi H n_\mathrm{d}\int\langle\mathbf{S}\rangle n R \, \mathrm{d}R \tag{34}$$

where

$$\langle\mathbf{S}\rangle = k_\mathrm{B}T(3\langle\mathbf{pp}\rangle - \mathbf{I}) + \frac{\pi\mu L^3\dot{\gamma}_0}{6\ln(2A)}\frac{R}{R_0}\left(\langle p_x p_z \mathbf{pp}\rangle - \frac{1}{3}\mathbf{I}\langle p_x p_z\rangle\right) \tag{35}$$

which is analogous to the expected stresslet of a dilute system of slender, Brownian rods in an unbound shear flow of rate $\dot{\gamma} = \dot{\gamma}_0 R/R_0$.[45]

Extracting the shear stress component $xz$ from eq 34 and normalizing by $n_\mathrm{d}L^3\mu\dot{\gamma}_0$ gives the particle stress contribution

$$\frac{\overline{\sigma}^P_{xz}}{n_\mathrm{d}L^3\mu\dot{\gamma}_0} = \frac{\overline{\sigma}^{PS}_{xz}}{n_\mathrm{d}L^3\mu\dot{\gamma}_0} + \frac{\overline{\sigma}^{PB}_{xz}}{n_\mathrm{d}L^3\mu\dot{\gamma}_0} \tag{36}$$

$$= \frac{2\pi^2 H}{6R_0\ln(2A)}\int\langle {p_x}^2 {p_z}^2\rangle n R^2 \, \mathrm{d}R + \frac{2\pi^2 H}{Pe_0\ln(2A)}\int\langle p_x p_z\rangle n R \, \mathrm{d}R \tag{37}$$

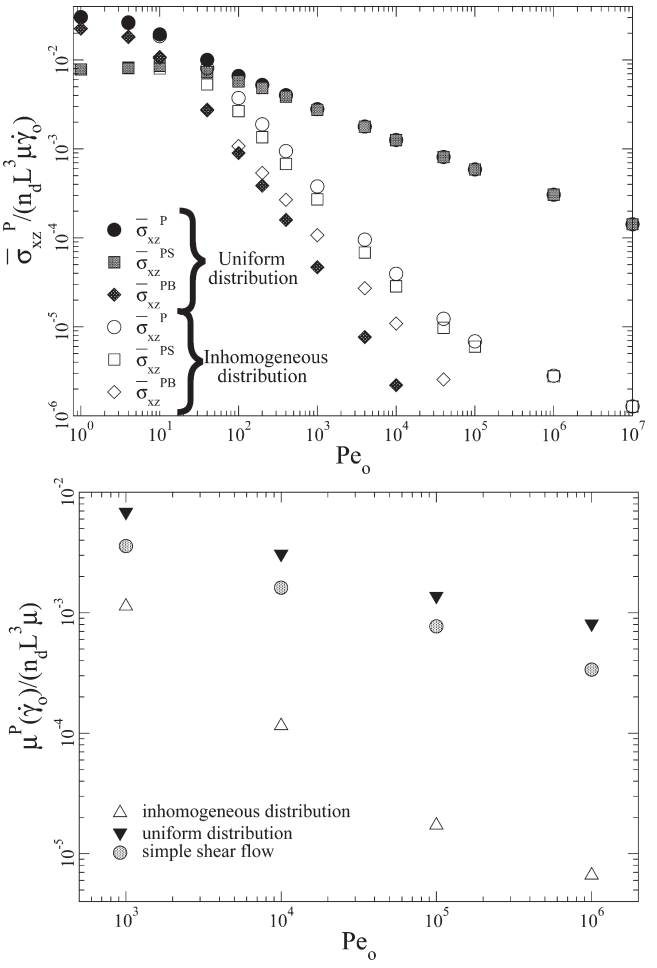


**Figure 6.** Comparisons of shear thinning caused by a rigid rod of $A = 10$ in torsional flow in terms of (top) the particle stress contributions $\bar{\sigma}_{xz}^{P}$ and (bottom) the apparent particle contribution to the viscosity $\mu^{P}(\dot{\gamma}_0)$ as a function of $Pe_0$ considering inhomogeneous distributions (open symbols) and a uniform distribution (closed symbols). The viscosities for the case of a simple shearing flow are also shown.

which is decomposed into the contribution from the shear flow, $\bar{\sigma}_{xz}^{PS}$, and the contribution from the Brownian torque, $\bar{\sigma}_{xz}^{PB}$. Using orientation moments as interpolated from the numerical results shown in Figure 3 and integrating eq 27 with $n$ obtained from eq 17 gives the particle stress contribution at steady state, while integration with the transient distributions gives the time-dependent stresses. Using the results of eq 36 in eq 26 and dividing by the rate of shear at the edge of the plates gives the apparent contribution of the particles to the viscosity, $\mu^{P}(\dot{\gamma}_0)$, as a function of the shear rate

$$\mu^{P}(\dot{\gamma}_0) = 2\frac{\bar{\sigma}_{xz}^{P}}{\dot{\gamma}_0} + \frac{\partial \bar{\sigma}_{xz}^{P}}{\partial \dot{\gamma}_0} \tag{38}$$

**Particle Stress at Steady State.** Particle stress contributions $\bar{\sigma}_{xz}^{P}$ are calculated from eq 36 for distributions $n$ that are spatially uniform and for the inhomogeneous distributions obtained from eq 17. The apparent particle contribution to the viscosity, $\mu^{P}(\dot{\gamma}_0)$, is calculated from eq 38 using the resulting value of $\bar{\sigma}_{xz}^{P}$. The results are shown as a function of $Pe_0$ in Figure 6. Shear thinning is apparent for the uniform distribution at all values of $Pe_0 > 1.0$. At small $Pe_0$, the shear thinning results from the reduction of the Brownian contribution to the particle stress. Increasing the $Pe_0$ beyond 100

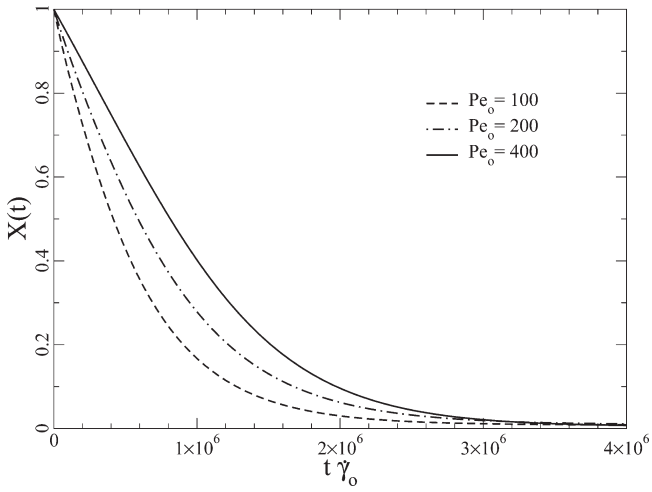


**Figure 7.** Extent of stress evolution $X(t)$ of a rigid rod of $A = 10$ in torsional flows of various $Pe_0$ with $R_0 = 100L$ as a function of time $t\dot{\gamma}_0$.

reduces the viscosity further, but primarily due to the shear component of the stress. The particle contribution to the viscosity is shown also for the case of simple shear in Figure 6. Comparing the viscosities demonstrates that a consistent difference exists between the values predicted for the uniform distribution in torsional flow and those predicted for simple shear due to the nonuniform shear rate in the torsional flow and despite using the correction given in eq 38.

The apparent shear thinning is magnified by the migration of rods toward the rotation axis. As shown in Figure 6, the shear thinning becomes more obvious as the $Pe_0$ increases since $n$ becomes more inhomogeneous. For relatively low $Pe_0$, the migration is not strong enough to significantly enhance the shear thinning observation. At $Pe_0 = 10^3$, however, the migration makes it appear as though the particle viscosity is nearly one-tenth the value of the particle viscosity for the uniform case. The discrepancy between the results continues to increase as $Pe_0$ increases.

**Particle Stress during Transient States.** Integrating eq 36 using the transient distributions obtained at each time $t$ in Figure 5 gives $\bar{\sigma}_{xz}^{P}(t)$, the time evolution of $\bar{\sigma}_{xz}^{P}$ with time. In Figure 7, the results are plotted in terms of the extent of stress evolution, which is defined as

$$X(t) = \frac{\bar{\sigma}_{xz}^{P}(t) - \bar{\sigma}_{xz}^{P}(t_s)}{\bar{\sigma}_{xz}^{P}(0) - \bar{\sigma}_{xz}^{P}(t_s)} \tag{39}$$

where $\bar{\sigma}_{xz}^{P}(0)$ corresponds to the particle stress contribution obtained from the uniform distribution and $\bar{\sigma}_{xz}^{P}(t_s)$ are the stresses obtained from the inhomogeneous distribution at steady state. As time proceeds, $X(t)$ decays from 1 and gradually approaches 0 as the distribution reaches steady state; as such, $X(t)$ provides a clearer measure of the time to steady state than comparing the distributions in Figure 5.

Figure 7 shows the effect of $Pe_0$ on $X(t)$. Realizing that time has been scaled by the shear rate within Figure 7, the time to achieve an extent $X(t)$ decreases at higher $Pe_0$ at the same $R_0$ as one would expect. The distributions all reach steady state by a time of $4 \times 10^6 \dot{\gamma}_0^{-1}$, as seen from the small values of $X(t)$ and consistent with the estimate given by eq 23.

Figure 8 shows that increasing $R_0$ results in a slower development of $X(t)$ since the rod must migrate larger distance to attain a steady distribution. For a so-called "rheometer-on-a-chip",[46,47] the ratio of disk radius to rod length could be as small as $R_0/L = 10^2$, in which case the

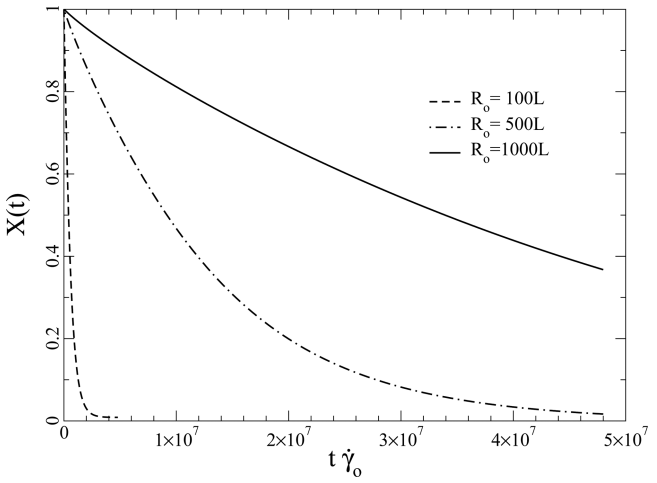


**Figure 8.** Extent of stress evolution $X(t)$ of a rigid rod of $A = 10$ in torsional flows of $Pe_0 = 100$ with various $R_0$ as a function of time $t\dot{\gamma}_0$.

system could approach steady state relatively quickly at sufficiently high $Pe_0$. However, the value of $R_0/L$ would be much larger than 100 in a typical rheological experiment. Considering nanotubes of length 1.0 $\mu$m sheared between disks having a radius of $R_0 = 2.0$ cm at $Pe_0 = 10^2$ gives a ratio of $R_0/L \sim 10^5$ and a very large time to steady state of $\sim O(10^{10})\dot{\gamma}_0^{-1}$. However, Figure 7 illustrates that even transient inhomogeneous distributions can give a large reduction in the stress at relatively short times for larger ratios of $R_0/L$.

## Conclusions

The dynamics and rheology of a Brownian, rigid rod in a torsional flow were investigated using kinetic theory. The relation between migration direction and rod orientation is clarified, showing that net migration requires breaking of the symmetry of the orientation distribution about the direction of flow. The center-of-mass distribution in the radial direction is also predicted from the equation of motion. Rigid rods are distributed toward the axis and more strongly at higher $Pe_0$. This distribution affects the particle stress contribution and results in an enhanced shear thinning.

The transient distributions and particle stress contributions show that shear thinning behavior observed in experiments[8] performed in torsional flow may be in part explained by the migration induced by the inhomogeneous velocity field. The results may seem to imply that rheological characterization of these systems using parallel plates is a poor choice, but other geometries commonly used for rheological testing have disadvantages as well. The inhomogeneous flow within both the Couette and cone-and-plate geometries will also induce a migration of rigid rods having finite Brownian fluctuations, though the extent of migration and impact upon the measurements requires investigation. Possible additional problems are introduced by the interactions of relatively large rods and the apex near the axis within the cone-and-plate geometry and the shear-induced migration from the gap to the region below the bob in the Couette geometry.

Experimental and simulation studies will improve our theoretical analysis in the context of the neglected effects, such as concentration, interactions with boundaries, and flexibility of particles. These will resolve the quantitative estimation of the time to achieve the steady state, which was found to be very large.

**Acknowledgment.** This work was supported by the National Science Foundation through a CAREER Award (CTS-0348205).

## Appendix

A Brownian dynamics algorithm is used to validate the approximation made within eq 6 and eq 22 by comparing the distribution calculated from an ensemble of single rod trajectories as a function of time against the theoretical prediction. The rod trajectories are calculated by performing a stochastic integration of the coupled equations for the orientation, eq 21, and center-of-mass, eq 13. The discretized equations are

$$\frac{R(t+\Delta t)-R(t)}{\Delta t} = -\frac{L^2\dot{\gamma}_0}{12R_0}p_x p_z + L\sqrt{\frac{\dot{\gamma}_0}{6Pe_0\Delta t}}(\hat{\mathbf{y}} + (\sqrt{2}-1)p_y\mathbf{p})\cdot\mathbf{w}_R \tag{40}$$

and

$$\frac{\mathbf{p}(t+\Delta t)-\mathbf{p}(t)}{\Delta t} = \frac{\dot{\gamma}_0}{R_0}Rp_z(\hat{\mathbf{x}} - p_x\mathbf{p}) + \sqrt{\frac{2\dot{\gamma}_0}{Pe_0\Delta t}}(\mathbf{I}-\mathbf{pp})\cdot\mathbf{w}_p - \frac{2\dot{\gamma}_0}{Pe_0}\mathbf{p} \tag{41}$$

The equations satisfy the fluctuation−dissipation theorem when the vectors $\mathbf{w}_R$ and $\mathbf{w}_p$ contain random numbers selected from a uniform distribution having zero mean and unit variance. Note that the last term in eq 41 is the divergence of the rotational diffusivity; this correction to the Euler method is required for an accurate solution to the stochastic equation as demonstrated by Cobb and Butler.[40] A similar term does not appear in eq 40 since the divergence of the center-of-mass diffusivity equals zero.

Only the radial position of the rod is considered in order to make a consistent comparison with the theoretical analysis which ignores the role played by the solid boundaries. In the event that a rod passes through the boundary at $R_0$ by an amount $\varepsilon$, the rod is repositioned at $R = R_0 - \varepsilon$; a similar reflection condition is used at the origin, though in this case the orientation must also be reset to maintain the proper orientation with respect to the direction of the flow.

Simulation results are shown in Figure 5 for the case of $Pe_0 = 100$ and $R_0 = 100L$. The mean values shown in the figure represent the distribution calculated from eight sets of numerical integrations consisting of 300 particles each; the error bars represent the standard deviation between the eight sets. The rods were initially distributed uniformly in the radial direction and were assigned a random orientation. A time step of $\Delta t = 1.0 \times 10^{-3}\dot{\gamma}_0^{-1}$ was sufficient for attaining a convergent result at $Pe_0 = 100$ as verified by lowering the time step by a factor of 10 and repeating the simulations.

## References and Notes

(1) Hough, L. A.; Islam, M. F.; Janney, P. A.; Yodh, A. G. *Phys. Rev. Lett.* **2004**, *93*, 168102.
(2) Davis, V. A.; Ericson, L. M.; Parra-Vasquez, A. N. G.; Fan, H.; Wang, Y. H.; Prieto, V.; Longoria, J. A.; Ramesh, S.; Saini, R. K.; Kittrell, C.; Billups, W. E.; Adams, W. W.; Hauge, R. H.; Smalley, R. E.; Pasquali, M. *Macromolecules* **2004**, *37*, 154–160.
(3) Parra-Vasquez, A. N. G.; Stepanek, I.; Davis, V. A.; Moore, V. C.; Haroz, V. C.; Shaver, J.; Hauge, R. H.; Smalley, R. E.; Pasquali, M. *Macromolecules* **2007**, *40*, 4043–4047.
(4) Chatterjee, T.; Krishnamoorti, R. *Macromolecules* **2008**, *41*, 5333–5338.
(5) Ganani, E.; Powell, R. L. *J. Compos. Mater.* **1985**, *19*, 194–215.
(6) Chaouche, M.; Koch, D. L. *J. Rheol.* **2001**, *45*, 369–382.
(7) Sepehr, M.; Carreau, P. J.; Moan, M.; Ausias, G. *J. Rheol.* **2004**, *48*, 1023–1048.
(8) Bricker, J. M.; Park, H.-O.; Butler, J. E. *J. Rheol.* **2008**, *52*, 941–955.

(9) Batchelor, G. K. *J. Fluid Mech.* **1971**, *46*, 813–829.
(10) Dinh, S. M.; Armstrong, R. C. *J. Rheol.* **1984**, *28*, 207–227.
(11) Shaqfeh, E. S. G.; Fredrickson, H. *Phys. Fluids A* **1990**, *2*, 7–24.
(12) Yamane, Y.; Kaneda, Y.; Doi, M. *J. Non-Newtonian Fluid Mech.* **1994**, *54*, 405–421.
(13) Sundararajakumar, R. R.; Koch, D. L. *J. Non-Newtonian Fluid Mech.* **1997**, *73*, 205–239.
(14) Bennington, C. P. J.; Kerekes, R. J.; Grace, J. R. *Can. J. Chem. Eng.* **1990**, *68*, 748–757.
(15) Aubert, J. H.; Tirrell, M. *J. Chem. Phys.* **1980**, *72*, 2694–2701.
(16) Aubert, J. H.; Prager, S.; Tirrell, M. *J. Chem. Phys.* **1980**, *73*, 4103–4112.
(17) Brunn, P. O. *J. Chem. Phys.* **1984**, *80*, 3420–3426.
(18) Brunn, P. O.; Chi, S. *Rheol. Acta* **1984**, *23*, 163–171.
(19) Happel, J.; Brenner, H. *Low Reynolds Number Hydrodynamics*; Prentice-Hall: Englewood Cliffs, NJ, 1965.
(20) Brenner, H. *Chem. Eng. Sci.* **1966**, *21*, 97–109.
(21) Karis, T. E.; Prieve, D. C.; Rosen, S. L. *J. Rheol.* **1984**, *28*, 381–392.
(22) Prieve, D. C.; Jhon, M. S.; Koenig, T. L. *J. Rheol.* **1985**, *29*, 639–654.
(23) Choi, H. J.; Prieve, D. C.; Jhon, M. S. *J. Rheol.* **1987**, *31*, 317–321.
(24) Choi, H. J. *Korean J. Rheol.* **1991**, *3*, 13–21.
(25) Feng, J.; Joseph, D. D. *J. Fluid Mech.* **1996**, *324*, 199–222.
(26) Ma, H.; Graham, M. *Phys. Fluids* **2005**, *17*, 083103.
(27) Butler, J. E.; Usta, O. B.; Kekre, R.; Ladd, A. J. C. *Phys. Fluids* **2007**, *19*, 113101.
(28) Park, J.; Bricker, J. M.; Butler, J. E. *Phys. Rev. E* **2007**, *76*, 040801.
(29) Doi, M.; Edwards, S. F. *The Theory of Polymer Dynamics*; Oxford University Press: New York, 1986.
(30) Bird, R. B.; Curtiss, C. F.; Armstrong, R. C.; Hassager, O. *Dynamics of Polymeric Liquids*; John Wiley & Sons: New York, 1987; Vol. *2*.
(31) Park, J.; Butler, J. E. *J. Fluid Mech.* **2009**, *630*, 267–298.
(32) Moran, J. P. *J. Fluid Mech.* **1963**, *17*, 285–304.
(33) Batchelor, G. K. *J. Fluid Mech.* **1970**, *44*, 419–440.
(34) Cox, R. G. *J. Fluid Mech.* **1970**, *44*, 791–810.
(35) Stover, C. A.; Koch, D. L.; Cohen, C. *J. Fluid Mech.* **1992**, *238*, 277–296.
(36) Nitsche, L. C.; Hinch, E. J. *J. Fluid Mech.* **1997**, *332*, 1–21.
(37) Schiek, R. L.; Shaqfeh, E. S. G. *J. Fluid Mech.* **1997**, *332*, 23–39.
(38) Harlen, O. G.; Sundararajakumar, R. R.; Koch, D. L. *J. Fluid Mech.* **1999**, *388*, 355–388.
(39) Butler, J. E.; Shaqfeh, E. S. G. *J. Fluid Mech.* **2002**, *468*, 205–237.
(40) Cobb, P. D.; Butler, J. E. *J. Chem. Phys.* **2005**, *123*, 054908.
(41) de Pablo, J. J.; Ottinger, H. C.; Rabin, Y. *AIChE J.* **1992**, *38*, 273–283.
(42) Morrison, F. A. *Understanding Rheology*; Oxford University Press: New York, 2001.
(43) Schiek, R. L.; Shaqfeh, E. S. G. *J. Fluid Mech.* **1995**, *296*, 271–324.
(44) Dhont, J. K. G.; Briels, W. J. *J. Chem. Phys.* **2003**, *118*, 1466–1478.
(45) Hinch, E. J.; Leal, L. G. *J. Fluid Mech.* **1976**, *76*, 187–208.
(46) Poole, R. J.; Alves, M. A.; Oliveira, P. J. *Phys. Rev. Lett.* **2007**, *99*, 164503.
(47) Pipe, C. J.; Majmudar, T. S.; McKinley, G. H. *Rheol. Acta* **2008**, *47*, 621–642.